

# Modeling the refractive index profile $n(z)$ of polar ice for ultra-high energy neutrino experiments

S. Ali,<sup>1</sup> P. Allison,<sup>2</sup> S. Archambault,<sup>3</sup> J.J. Beatty,<sup>2</sup> D.Z. Besson,<sup>1</sup> A. Bishop,<sup>4</sup> P. Chen,<sup>5</sup> Y.C. Chen,<sup>5</sup> B.A. Clark,<sup>6</sup> W. Clay,<sup>7</sup> A. Connolly,<sup>2</sup> K. Couberly,<sup>1</sup> L. Cremonesi,<sup>8</sup> A. Cummings,<sup>9,10,11</sup> P. Dasgupta,<sup>2</sup> R. Debolt,<sup>2</sup> S. de Kockere,<sup>12</sup> K.D. de Vries,<sup>12</sup> C. Deaconu,<sup>7</sup> M. A. DuVernois,<sup>4</sup> J. Flaherty,<sup>2</sup> E. Friedman,<sup>6</sup> R. Gaior,<sup>3</sup> P. Giri,<sup>13</sup> J. Hanson,<sup>14</sup> N. Harty,<sup>15</sup> K.D. Hoffman,<sup>6</sup> J.J. Huang,<sup>5</sup> M.-H. Huang,<sup>5,16</sup> K. Hughes,<sup>2</sup> A. Ishihara,<sup>3</sup> A. Karle,<sup>4</sup> J.L. Kelley,<sup>4</sup> K.-C. Kim,<sup>6</sup> M.-C. Kim,<sup>3</sup> I. Kravchenko,<sup>13</sup> R. Krebs,<sup>9,10</sup> C.Y. Kuo,<sup>5</sup> K. Kurusu,<sup>3</sup> U.A. Latif,<sup>12</sup> C.H. Liu,<sup>13</sup> T.C. Liu,<sup>5,17</sup> W. Luszczyk,<sup>2</sup> K. Mase,<sup>3</sup> M.S. Muzio,<sup>9,10,11</sup> J. Nam,<sup>5</sup> R.J. Nichol,<sup>8</sup> A. Novikov,<sup>15</sup> A. Nozdrina,<sup>1</sup> E. Oberla,<sup>7</sup> Y. Pan,<sup>15</sup> C. Pfendner,<sup>18</sup> N. Punsuebsay,<sup>15</sup> J. Roth,<sup>15</sup> A. Salcedo-Gomez,<sup>2</sup> D. Seckel,<sup>15</sup> M.F.H. Seikh,<sup>1</sup> Y.-S. Shiao,<sup>5,19</sup> D. Smith,<sup>7</sup> S. Toscano,<sup>20</sup> J. Torres,<sup>2</sup> J. Touart,<sup>6</sup> N. van Eijndhoven,<sup>12</sup> A. Vieregge,<sup>7</sup> M.-Z. Wang,<sup>5</sup> S.-H. Wang,<sup>5</sup> S.A. Wissel,<sup>9,10,11</sup> C. Xie,<sup>8</sup> S. Yoshida,<sup>3</sup> and R. Young<sup>1</sup>

(ARA Collaboration)

<sup>1</sup>Dept. of Physics and Astronomy, University of Kansas, Lawrence, KS 66045

<sup>2</sup>Dept. of Physics, Center for Cosmology and AstroParticle Physics, The Ohio State University, Columbus, OH 43210

<sup>3</sup>Dept. of Physics, Chiba University, Chiba, Japan

<sup>4</sup>Dept. of Physics, University of Wisconsin-Madison, Madison, WI 53706

<sup>5</sup>Dept. of Physics, Grad. Inst. of Astrophys., Leung Center for Cosmology and Particle Astrophysics, National Taiwan University, Taipei, Taiwan

<sup>6</sup>Dept. of Physics, University of Maryland, College Park, MD 20742

<sup>7</sup>Dept. of Physics, Enrico Fermi Institute, Kavli Institute for Cosmological Physics, University of Chicago, Chicago, IL 60637

<sup>8</sup>Dept. of Physics and Astronomy, University College London, London, United Kingdom

<sup>9</sup>Center for Multi-Messenger Astrophysics, Institute for Gravitation and the Cosmos, Pennsylvania State University, University Park, PA 16802

<sup>10</sup>Dept. of Physics, Pennsylvania State University, University Park, PA 16802

<sup>11</sup>Dept. of Astronomy and Astrophysics, Pennsylvania State University, University Park, PA 16802

<sup>12</sup>Vrije Universiteit Brussel, Brussels, Belgium

<sup>13</sup>Dept. of Physics and Astronomy, University of Nebraska, Lincoln, Nebraska 68588

<sup>14</sup>Dept. Physics and Astronomy, Whittier College, Whittier, CA 90602

<sup>15</sup>Dept. of Physics, University of Delaware, Newark, DE 19716

<sup>16</sup>Dept. of Energy Engineering, National United University, Miaoli, Taiwan

<sup>17</sup>Dept. of Applied Physics, National Pingtung University, Pingtung City, Pingtung County 900393, Taiwan

<sup>18</sup>Dept. of Physics and Astronomy, Denison University, Granville, Ohio 43023

<sup>19</sup>National Nano Device Laboratories, Hsinchu 300, Taiwan

<sup>20</sup>Universite Libre de Bruxelles, Science Faculty CP230, B-1050 Brussels, Belgium

(Dated: November 15, 2024)

We have developed an *in-situ* index of refraction profile  $n(z)$  for cold polar ice, using the transit times of radio signals broadcast from an englacial transmitter to 2-5 km distant radio-frequency receivers, deployed at depths up to 200 m. For propagation through a non-uniform medium, Maxwell's equations generally admit two ray propagation solutions from a given transmitter, corresponding to a direct path (D) and a refracted or reflected path (R); the measured D vs. R timing differences ( $dt(D,R)$ ) are determined by the refractive index profile. We constrain  $n(z)$  near South Pole, where the Askaryan Radio Array (ARA) neutrino observatory is located, by simulating D and R ray paths via ray tracing and comparing simulations to measured  $dt(D,R)$  values. Using previous ice density data as a proxy for  $n(z)$ , we demonstrate that our data strongly favors a glaciologically-motivated three-phase densification model rather than a single exponential scale height model. Effective volume simulations for a detector of ARA station antenna depths yield a 14% increase in neutrino sensitivity over a range of  $10^{17} - 10^{21}$  eV using the three-phase model compared to a single exponential.

## I. INTRODUCTION

Ultra-High Energy Neutrino (UHEN) experiments such as the Radio Neutrino Observatory in Greenland (RNO-G), the Askaryan Radio Array (ARA), and the proposed IceCube Gen-2 experiment seek to extend the energy window of observed neutrinos beyond the MeV (typical of solar neutrinos) and PeV scales (astrophysical, as observed by IceCube) to  $>PeV$  ('cosmogenic')

energy scales [1–3]. Radio detection provides a cost-effective method for constructing detectors with a large sensitive volume, as radio signals propagate farther in ice compared to optical signals. A major motivation of UHEN experiments is to complement observations of ultra-high energy charged cosmic rays (UHECR) from distant astronomical sources. UHEN are emitted following collisions of UHECR with matter or the Cosmic Microwave Background. Due to their lack of charge and

small cross-section, neutrinos are able to propagate, undeflected, through obstacles otherwise opaque to gamma or cosmic rays. However, these same weakly interacting characteristics render observation difficult.

Radio propagation in ice, over kilometer-long distance scales, is essential for the radio neutrino experiments. Since, as the neutrino energy increases, the expected neutrino flux sharply decreases, radio neutrino experiments must scan over large volumes for long exposure times to achieve measurable neutrino event rates.

Simulations which incorporate models of the complex-valued ice permittivity are used to estimate the sensitivity of UHEN experiments. The real part of the complex permittivity dictates the ray path followed by radio signals, from interaction point to receiver, while the imaginary part quantifies the degree to which signal is absorbed in-ice. Given the non-magnetic nature of ice, the permittivity relates directly to the refractive index profile through  $n = \sqrt{\epsilon_r}$  where  $\epsilon_r$  is the real part of the ice permittivity. Since the overburden increases with depth, UHEN experiments assume a depth-dependent refractive index ansatz. For a given receiver, the varying index of refractive profile in the upper  $\sim 100$ - $150$ m generates, by Fermat's Least Time Principle, curved rather than rectilinear ray trajectories. Given a receiver depth, this ray-bending results in a 'shadowed' volume within which neutrino interactions will be inaccessible - this loss of sensitivity is increasingly important for large horizontal displacements and shallow receivers. As the depth of deployed receiver decreases (i.e., receiver gets closer to the surface) the extent of the shadowed zone is an increasingly important determinant of the neutrino interaction volume visible to a given receiver, and therefore the number of detected neutrinos.

The simplest ansatz for the refractive index profile is one that follows a single exponential dependence on depth, as expected for a self-gravitating fluid. Glaciological studies of ice density as a function of depth, however, suggest that densification occurs in multiple stages [4–6]. Using ARA receiver timing data obtained in response to a pulser lowered into the ice, we have tested a piece-wise function separated into these 3 stages against a simpler one-stage or two-stage exponential model.

## II. ICE DENSIFICATION AND THE REFRACTIVE INDEX

Our model assumes a linear dependence of refractive index on density[7], although this relationship has not yet been fully verified in the lab. According to Sorge's Law [8], density is constant over time at a given depth, assuming constant snow accumulation and constant temperature. (In reality, the snow accumulation and temperature conditions are not constant, which leads to density fluctuations; in what follows, we neglect such effects, as well as the possible effect of impurities.) In a scale-height model, the densification rate of snow is taken to be pro-

portional to the change in pressure due to the weight of the snow overburden, leading to the exponential form

$$\rho(z) = \rho_f - b_0 e^{Cz} \quad (1)$$

where  $\rho_f$  is the density of deep ice,  $\rho_f - b_0$  is the density of snow at the surface, and  $C$  is a proportionality constant prescribed by the densification rate. The density profile  $\rho(z)$  can then be translated to  $n(z)$  assuming a linear relationship between the two quantities.

Theoretical and empirical models of ice density as a function of depth, however, prescribe two boundaries that affect the ice densification rate as  $\rho(z)$  crosses certain thresholds[6, 9]. The (better-studied) first boundary at  $\sim 550$  kg/m<sup>3</sup>[4] separates the snow and firn regions, and occurs at depths of  $\sim 15$ m and  $\sim 20$ m for Summit and South Polar ice, respectively.[5]. A second boundary separates the firn and bubbly ice regions. The ice is considered to be fully formed in the third region, but there still exist air pockets within the ice that reduce the overall density relative to  $\rho_f$ . These air pockets are crushed under greater pressure as depth increases, asymptotically reaching the  $\rho_f \sim 920$  kg/m<sup>3</sup> density of typical pure, deep ice at  $T = -30^\circ$  C[10]. To account for changing densification rates in the separate regions, the form of Eqn (1) is modified to a piecewise function.

$$\rho < \rho_1 : \rho(z) = \rho_f - b_0 e^{c_1 z}$$

$$\rho_1 \leq \rho < \rho_2 : \rho(z) = \rho_f - b_1 e^{c_2(z-z_1)}$$

$$\rho \geq \rho_2 : \rho(z) = \rho_f - b_2 e^{c_3(z-z_2)} \quad (2)$$

where  $\rho_1$  and  $\rho_2$  are density boundary conditions that define the regions,  $b_0, b_1$  and  $b_2$  are determined by surface density and continuity at each boundary, and  $c_1, c_2$  and  $c_3$  are constants describing the densification rate in each density region.

Figure 1 shows ice density data taken from a number of sites near Summit Station, Greenland. This density data approaches the asymptotic value and therefore includes measurements well into the expected bubbly ice region. A best fit model to the combined density data is shown using a piece-wise function following the form of Eqn. (2). The 550 kg/m<sup>3</sup> boundary between the snow and firn regions is based on previous studies [4, 5], while the boundary between firn and bubbly ice is determined empirically by fitting the  $\rho(z)$  data for the inflection point separating the intermediate and highest density regions, using the Levenberg–Marquardt fitting algorithm[11]. This empirically fit gives a 758 kg/m<sup>3</sup> boundary between the firn and bubbly ice regions which is used as to determine the second depth boundary in Eqn. (6). Past studies of the snow to bubbly ice density boundary have used a density from 800-830 kg/m<sup>3</sup> [4, 9].

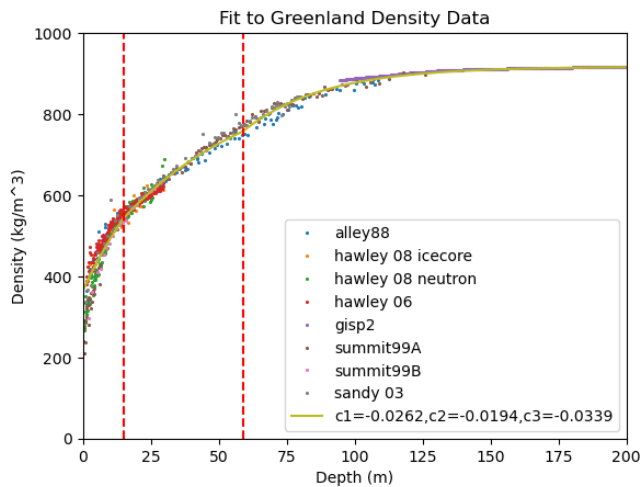


FIG. 1. Fits to indicated parameterization of Greenland ice density;  $c_1, c_2, c_3$  refer to the exponential parameters for the snow, firn, and bubbly ice regions, respectively. Red dotted lines (14.9m, 58.9m) separate the three regimes. Greenland ice density data have been taken from [12–15].

### A. Calculating refractive index from density

As mentioned previously, ice density is converted to index of refraction  $n(z)$  using a linear relationship based on studies of dielectric constant vs. specific gravity at both Maudheim and also the McMurdo ice shelf [7, 16]:

$$n(z) = 1 + A\rho, \quad (3)$$

where  $\rho$  is the pure ice specific-gravity and  $A$  is a proportionality constant, which can be estimated from the constraint that deep, bulk ice has a refractive index corresponding to the measured value at a given site. At Summit Station, Greenland,  $n=1.778 \pm 0.006$  [10] for bulk ice. Different fits to McMurdo ice shelf data give  $A$  values ranging from 0.840-0.858. Application of Eqn. (2) translates the exponentially-assumed density data into a two-parameter exponential  $n(z)$  profile, customarily written as:

$$n(z) = 1.778 - be^{Cz}. \quad (4)$$

Figure 2 shows single exponential fits as well as 3-stage piece-wise exponential fits for which the 3-stage model uses Eqn. (3) to solve for density at the transition points separating the three densification regions. (Since there are fewer density measurements in the bubbly ice region, the third exponential parameter of the SPICE based model described below is estimated directly from the data itself, as outlined in Section VI.)

The density data are converted to refractive index using equation (2) with a constant  $A = 0.845$  found by the McMurdo ice shelf study [16] and consistent with

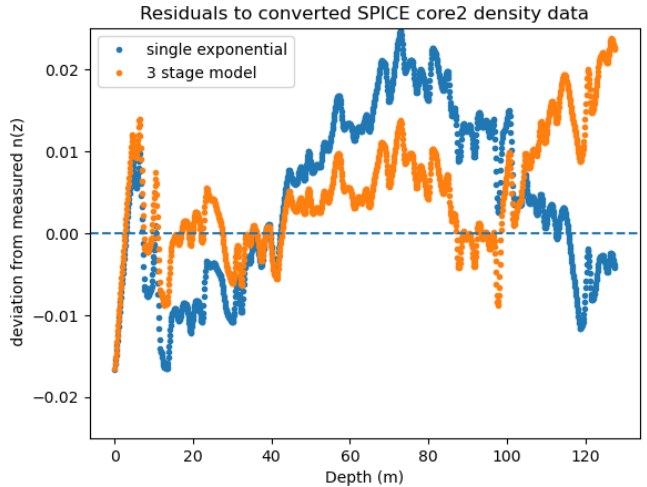
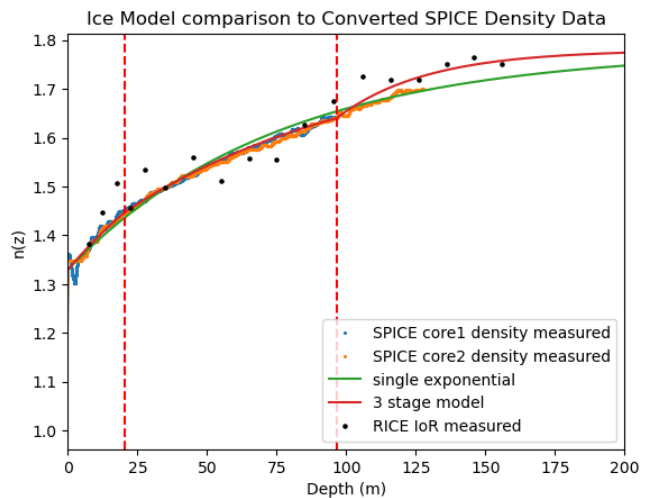


FIG. 2. Density profiles corresponding to Equations (5) (single exponential) and (6) (3 stage model) compared to SPICE density data [17] down to 127m depth. Deviation between the two SPICE core density measurements suggest an error of  $\pm 0.005$  in measured  $n(z)$  values. The 3 stage model  $c_3$  parameter is constrained by SPICE  $dt(D,R)$  data (see Section VI).

measurements from Summit Station, Greenland, assuming the  $920 \text{ kg/cm}^3$  asymptotic density observed in deep Antarctic and Greenlandic ice [9, 18].

Relative to a single exponential, Figure 2 illustrates how partitioning the model into 3 separate exponential functions allows for an improved density fit, relative to the single exponential functions often used in current simulations. Including the region where the  $c_3$  parameter constrained by SPICE  $dt(D,R)$  data (see Section VI) deviates from the limited converted density data, Eqn. (6) improves the RMS of the density data points from 0.0112 to 0.0085 over Eqn. (5).

## B. Experimental Layout

Analyzed ARA data discussed below were drawn from multiple, and redundant combinations of transmitters and receivers, spanning in-ice transmitter depths of up to 1.5 km and horizontal trajectories of up to 5 km, over a wide range of incidence angles. A plane view of the relevant radio-frequency instrumentation in the vicinity of South Pole is presented in Figure 3, showing the receiver stations relative to the radio-frequency transmitters.

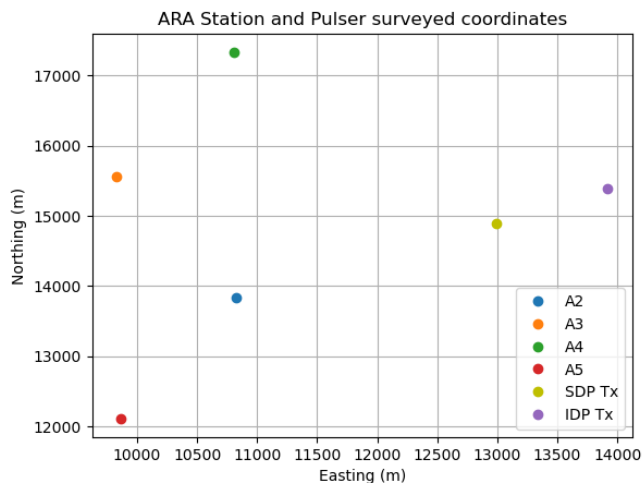


FIG. 3. Experimental layout. Surveyed coordinates in Easting, Northing for ARA stations A2, A3, A4 and A5 for which timing data from the SPICE (SDP) and IC1S (IDP) are analyzed. The SDP transmitter was lowered from the surface to a depth of 1700 m, and the IDP transmitter was at a fixed depth of approximately 1400 m.

## C. SPICE

The South Pole Ice Core (SPICE) borehole was drilled to 1751m over the 2014-2015 and 2015-2016 austral seasons with the purpose of collecting data to determine changes in atmospheric chemistry, climate, and biogeochemistry since the most recent [40 ka] glacial-interglacial cycle [19]. Proximal to the ARA stations, SPICE offers both density data and also the opportunity for deep pulser timing measurements. Figure 2 shows the 3 stage and single exponential models based on converted density data drawn from the SPICE borehole. In the case of SPICE fits, we compare a single exponential

$$n(z) = 1.778 - 0.45e^{-0.0132z} \quad (5)$$

to the 3 stage model parameterization, corresponding to the snow, firn, and bubbly ice regions, respectively:

$$z < 20.5\text{m} : n(z) = 1.778 - 0.45e^{-0.0148z}$$

$$20.5\text{m} \leq z < 96.6\text{m} : n(z) = 1.778 - 0.33e^{-0.0114(z-20.5)}$$

$$z \geq 96.6\text{m} : n(z) = 1.778 - 0.14e^{-0.029(z-96.6)} \quad (6)$$

taking  $z$  to be positive and increasing with depth. The exponentials in the firn and bubbly ice regions are shifted in depth to begin at the start of their respective regions instead of the surface; the constants  $c_1$ ,  $c_2$ , and  $c_3$  refer to the constant terms in the exponent for  $e^{cz}$ , in each densification regime. For both Eqns. (5) and (6), the asymptotic density of pure ice is fixed at 1.778 and  $b_1$  is fixed by the surface density. The remaining parameters  $b_2$  and  $b_3$  (Eqn. (2)) are constrained by continuity while  $c_1$  and  $c_2$  are fit to the converted SPICE density data. The final parameter  $c_3$  is determined from the deep pulser data.

A previous study of radio propagation in ice in Greenland used a two-stage parameterization similar to Eqn. (6) using only the snow to firn boundary [20]. Fitting the 2 stage parameterization to the existing converted SPICE density data gives:

$$z < 20.5\text{m} : n(z) = 1.778 - 0.45e^{-0.0148z}$$

$$z \geq 20.5\text{m} : n(z) = 1.778 - 0.33e^{-0.0117(z-20.5)} \quad (7)$$

We now discuss verification of the proposed model (Eqns. (5), (6), and (7)) using ARA deep pulser data.

## III. DEEP PULSER DATA

A typical ARA station is shown in Figure 4; ARA consists of 5 such stations, denoted as ‘A1’-‘A5’. Each station consists of 4 boreholes at the vertices of a horizontal square, with an inter-string lateral separation of order 20 meters; each borehole contains a vertical string of radio receiver antennas. Each string consists of 2 horizontally polarized (Hpol) and 2 vertically polarized (Vpol) antennas. This allows the stations to record both Hpol and Vpol signals, as well as infer the polarization of a signal based on the relative amplitudes of the signals registered on the Hpol vs. Vpol antennas. The array of antennas allows for the reconstruction of a source location based on the relative timings for signals received by multiple antennas. For a typical station, the top Hpol to bottom Vpol antennas are deployed at depths ranging from 170-200m. Nearby englacial pulsers are used to calibrate channel positions and accuracy using relative timing differences, assuming some  $n(z)$  profile.

In our case, we are interested in not only the direct (D) signal arrival time, but also the arrival time of the refracted/reflected (R) signal arrival time. Calculating these values from either the leading edges of the observed signals or a cross-correlation, we can calculate the timing difference  $dt(D,R)$ .

The  $dt(D,R)$  timing difference offers several advantages in calibration.  $dt(D,R)$  is immune to data acquisition signal transmission (aka ‘cable delay’) uncertainties since

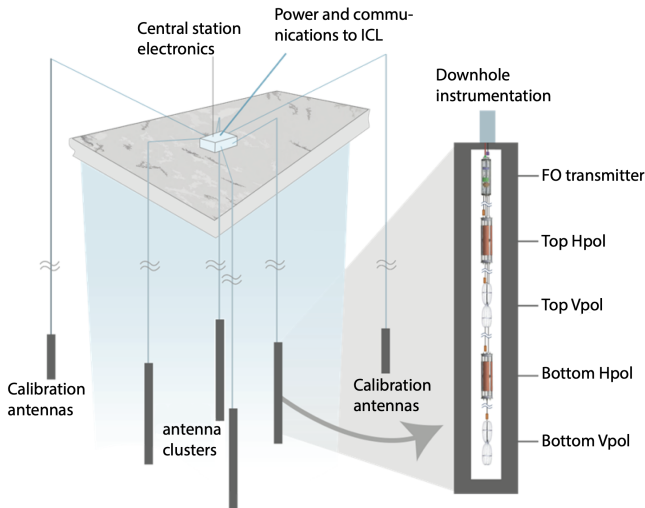


FIG. 4. ARA station layout, comprising 16 antennas (8 Hpol and 8 Vpol) ranging from 170–200m depths.

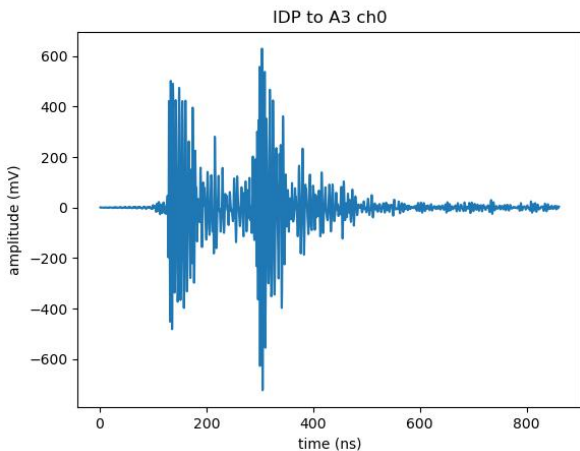


FIG. 5. Example stationary IceCube deep pulser (IDP) averaged waveform at 1400m depth, illustrating the direct (first) and refracted (second) signals measured in ARA station A3.

the cable delays are equal for the D and R signals on a single channel waveform capture. The  $dt(D,R)$  method is also particularly useful for testing  $n(z)$  models due to the differences between the D and R optical paths (see Figure 6). The R ray path travels through ice well above the receiver antenna which allows for testing a greater range of depths for  $n(z)$ . By contrast, nearby calibration pulsers only test  $n(z)$  over the limited depth range of the deployed ARA antennas. From a science perspective, since  $dt(D,R)$  (approximately) linearly depends on the range to source location, it can also be used as a powerful constraint in neutrino reconstruction, independent of conventional interferometric techniques to locate interaction points [21].

Figure 5 shows a 128-event average waveform obtained

from a stationary deep pulser deployed in one of the ice-holes drilled for the IceCube experiment (referred to as ‘IceCube Deep Pulser’, or ‘IDP’;  $z=1400$  m). The deep pulser is horizontally displaced from the ARA receiver station by typical distances of 1–5 km, depending on the ARA receiver station. This IDP source signal was observed in all 5 ARA stations. Additional data from a deep pulser lowered into the SPICE borehole in the 2018–2019 seasons (referred to as SDP) is also useful in discriminating between refractive index models. The South Pole University of Kansas Pressure Vessel Antenna, or SPUNK PVA transmitter antenna was deployed into the SPICE borehole located 2–4 km from stations A2–A5 [17]. This deep pulser source emitted 1 pulse per second (pps) signals to a depth of approximately 1700m. Stations began receiving double pulse (D,R) signals once the transmitter emerged from the shadow zone (around a depth of 500–700m, depending on the receiver station) resulting in a dataset of  $dt(D,R)$  pulses recorded to  $z=1300$ m. A more detailed description of the SPICE pulsing runs and received signals can be found in the literature [17]. Since the D and R ray paths differ over this range, this dataset provides a check on the consistency of  $n(z)$  models.

#### IV. SIMULATED DEEP PULSER SIGNALS

Ray paths, originating at either the IDP or SDP transmitters, are simulated using the numerical ray tracer **RadioPropa** [22], which calculates the two possible solutions (D and R), given source and receiver positions and some  $n(z)$  model. The travel time is calculated for each of the ray paths, and  $dt(D,R)$  is calculated directly from the difference in travel time for the two paths. Figure 6 shows the simulated ray paths from a 1300m deep source to an ARA antenna. The D ray path travels only through the bubbly ice region while the R path travels through both the bubbly ice and firm regions of the 3 stage model. Figure 7 shows the relative path lengths in each region of the simulated R ray path over a range of SPICE depths. As the apex of the R path approaches the firm to bubbly ice boundary the discontinuous gradient of the piecewise function results in a lack of simulated D and R solutions for this transmitter depth. This results in the gap in simulated values seen in Figure 7.

The ray tracing code **RadioPropa** is incorporated into **NuRadioMC**, a complete Monte Carlo simulation suite that can be used to simulate signal waveforms and determine the neutrino detection volume for a given radio neutrino detector configuration [23]. In addition to relative signal arrival times, simulated waveforms can be compared to the measured waveforms in terms of the relative amplitudes of the D and R signals as well as frequency content. In what follows we consider only timing information, although amplitude analysis is currently underway.



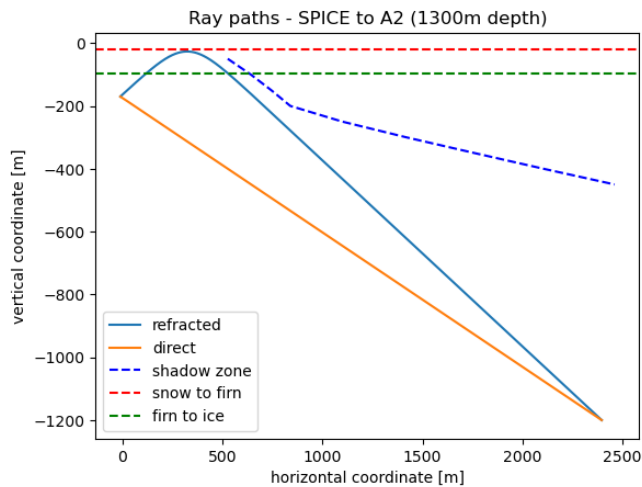


FIG. 6. Sample simulated (using Eqn. (6)) direct and refracted ray paths from a 1300m deep pulser in the SPICE borehole to channel 0 of ARA station A2. Horizontal dotted lines refer to the boundaries between regions of the 3 stage  $n(z)$  model. Shadow zone refers to the transmitter depth and distance boundary beyond which no signal reaches the receiver antenna.

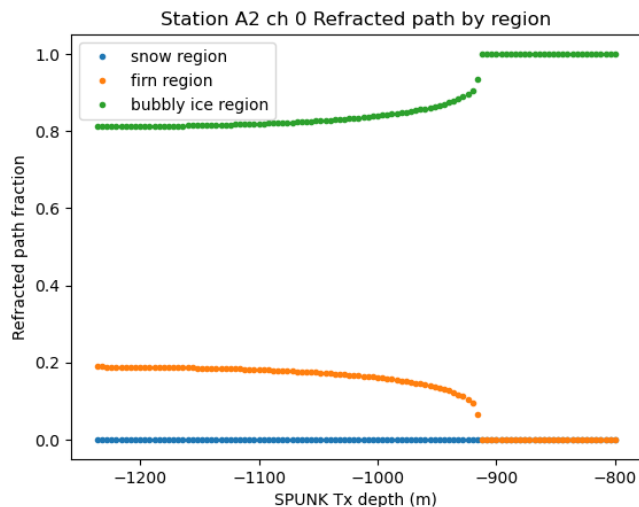


FIG. 7. Fraction of simulated (using Eqn. (6)) refracted ray path in the snow, firm, and bubbly ice regions from SPICE to station A2 channel 0 (170m depth) for various SPICE transmitter depths.

## V. SNOW ACCUMULATION IMPACT ON REFRACTIVE INDEX PROFILE

Before comparing our simulated  $dt(D,R)$  to data, it is important to consider possible effects of snow accumulation with time, since ARA receiver depths were recorded at the time of initial deployment (2011–2013 for stations A1–A3), while SDP pulser data were recorded in December, 2018. Yearly snowfall at the South Pole increases the overall depths, relative to the surface, of antennas buried

in prior years. A study at South Pole from 1983-2010 using a near-surface snow stake field near Amundsen-Scott station [24] found an average annual snow accumulation rate of 274.85 mm per year with a (non statistically-significant) downward trend of  $-2.8 \pm 6.7$  mm in annual accumulation over that time. However, over multiple years the increment for sub-surface antennas should be smaller than the annual accumulation at the surface due to the densification of snow to ice over time.

ARA Station A3 was deployed during the 2012-2013 season, two years after the IceCube deep pulsers were deployed. The SPICE borehole data were taken in the 2018-2019 season, corresponding to 6 years of snow accumulation since the initial antenna depths were recorded. Applying 6 years of accumulation using the 274.85 mm surface accumulation average implies an estimated 1.57 m of snow accumulation over this period. We can also estimate the snow accumulation at antenna depth by comparing  $dt(D,R)$  times for signals from one of the two IDP transmitters broadcast to ARA station A3, registered over a multi-year time period. Figure 8 overlays the Direct and Refracted signals for data recorded over an 8 year timespan. In contrast to the nearly-constant Direct signals, the Refracted signals, with much shallower trajectories, show clear discrepancies. The constancy of the Direct signals over time indicate that the variations in the observed Refracted waveforms are not the result of, e.g., hole closure effects or some other effect leading to a change in the antenna response over this timescale.

Combining data from several years and selecting those channels with the highest Signal-to-Noise Ratio, Figure 9 shows the extracted  $dt(D,R)$  times from the IC22S IDP to station A3 for 2015, 2018, and 2022 data. Averaged over all channels, the measured  $dt(D,R)$  from IC22S to A3 shows an increase of 6.9 ns (0.99 ns per yr) from 2015-2022 and an increase of 3.7 ns (0.93 ns per yr) from 2018-2022. Using RadioPropa’s numerical ray tracer we simulate the  $dt(D,R)$  times from IC22S to A3 and increase the depths of both the pulser and the station antennas to match the increased measured  $dt(D,R)$ . The measured  $dt(D,R)$  increases correspond to snow accumulations of 1.72 m (0.245 m per yr) from 2015-2022 and 0.936 m (0.234 m per yr) from 2018-2022 using the 3 stage model (5) to simulate  $dt(D,R)$ . In comparison, the 1983-2010 average surface snow accumulation would predict 1.82 m (0.26 m per yr) from 2015-2022 and 1.07 m (0.27 m per yr) from 2018-2022. The 2015-2022 and 2018-2022 IC22S data imply an average annual snow accumulation of  $0.24 \pm 0.09$  m (statistical errors only). We use this measured snow accumulation rate to correct station antenna depths recorded during deployment to the depths at the time of SPICE borehole data collection. Given the constant position of the IDP and channels relative to one another, the snow accumulation measurement also provides an estimate of the measured  $dt(D,R)$  uncertainty since snow accumulation should be equal across localized channels. Based on the statistical uncertainty between channels, we estimate measured  $dt(D,R)$  systematic er-

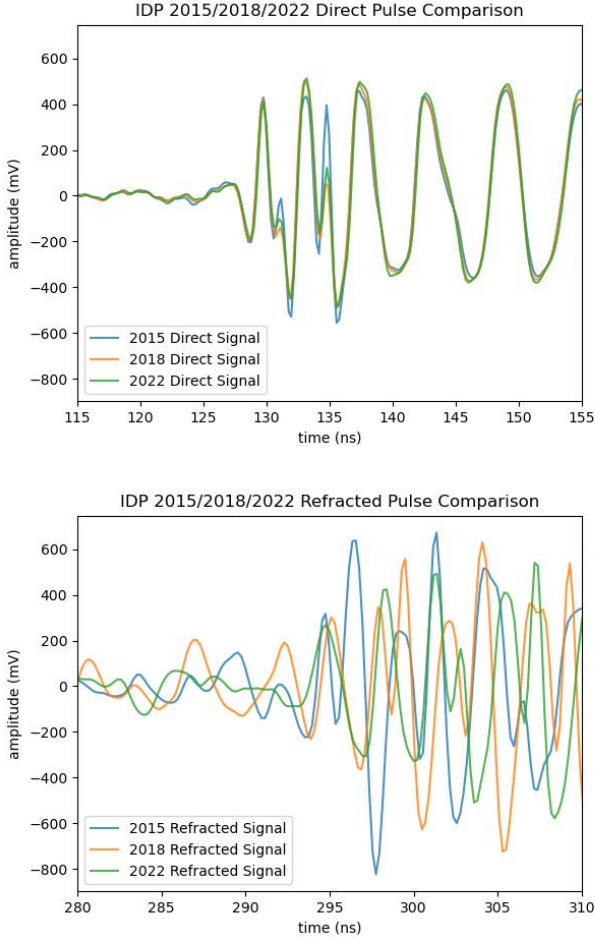


FIG. 8. Comparison of 2015 vs. 2018 vs. 2022 IceCube Deep Pulsar signals, showing Direct (top) and Refracted (bottom) signals. For the receiver channel considered (at a depth of 175 meters, and therefore close to the asymptotic ice density regime), the Direct signals are remarkably consistent with each other (indicating very little aging or hole closure effects), while the Refracted signals, which sample shallower snow and are more sensitive to refractive index changes, show evident differences.

ror of  $\pm 0.85$  ns arising from snow accumulation effects.

## VI. ICE MODEL RESULTS

By lowering a pulser into the SPICE borehole,  $dt(D,R)$  data were collected for a variety of ray paths. To ensure the transmitter is well beyond the shadow zone, we measure  $dt(D,R)$  over the depth range from 700–1300 m for most stations. Typical horizontal separations are of order 1–5 km - in the case of A3, for example, the SPICE borehole is laterally displaced 3230m. A sample A2 VPol waveform used for analysis is shown in Figure 10; in this case, the transmitter was located at a depth of 1077 m.

Fixing  $c_1$  and  $c_2$  to values obtained from fits to SPICE

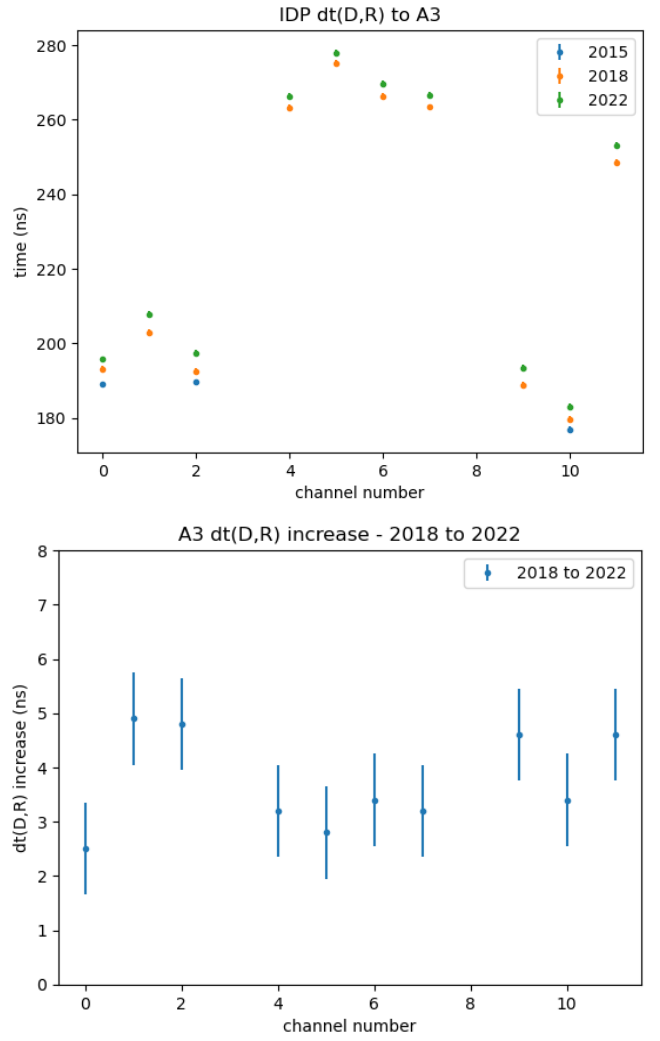


FIG. 9. Measured  $dt(D,R)$  from IDP to A3 antennas for 3 seasons (top) and relative increment in  $dt(D,R)$  (bottom); as expected,  $dt(D,R)$  increases for later seasons in accordance with increased antenna depth due to snow accumulation. The highest SNR channels 0,2,10 provide  $dt(D,R)$  data across all 3 seasons while remaining channels include  $dt(D,R)$  data only for the 2018 and 2022 seasons.

density data,  $c_3$  of Eqn. (6) was separately determined via  $\chi^2$  minimization between the measured and simulated  $dt(D,R)$  ( $\Delta dt(D,R)$ ) for the ‘unblinded’ station A2 only; that  $c_3$  value was then applied to simulations of the remaining stations. Figure 11 shows the normalized summed station A2  $\chi^2$  value (simulated, relative to measured  $dt(D,R)$  data) for various  $c_3$  values, around the minimum value.

Figure 12 shows the  $\Delta dt(D,R)$  distribution for SPICE broadcasts to ARA station A2 for the  $n(z)$  models corresponding to Eqns. (5) (single exponential), (6) (3 stage model), and (7) (2 stage model). ‘Measured’ times refer to  $dt(D,R)$  calculated using the arrival times of the D and R signals in double pulse waveforms similar to Figure 5, and are determined both by the crossing of an amplitude

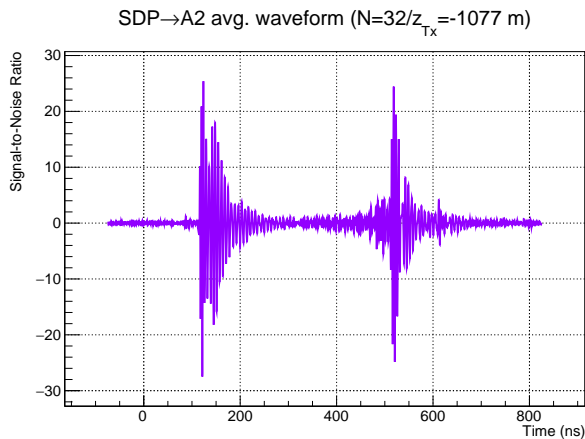


FIG. 10. Typical waveform recorded during SPICE transmitter run; Direct and Refracted pulses are evident in the Figure.

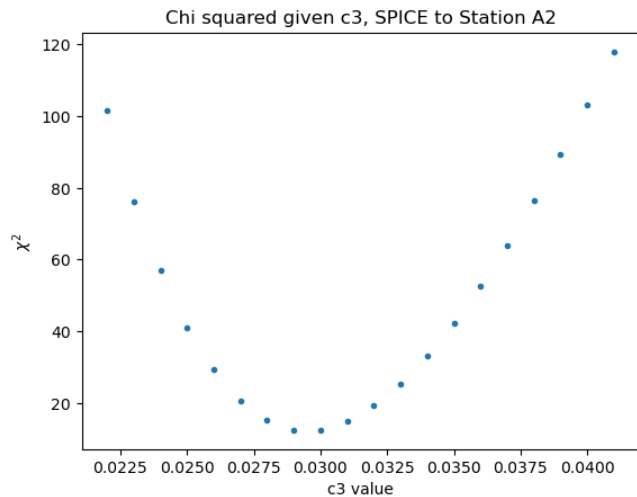


FIG. 11. Distribution of summed  $\chi^2$  of deviation between simulated and measured  $dt(D,R)$  ( $\Delta dt(D,R)$ ) for a given  $c3$  parameter using  $c1, c2$  of Eqn. (6), for all VPol channels of station A2.  $\chi^2$  is defined by the square of  $\Delta dt(D,R)$  divided by the error in the measured data. This fitted value of  $c3$  is then applied to the independent data collected with the remaining ARA receiver stations.

threshold as well as cross correlation of the D and R signals. A comparison of independent timing method gave a discrepancy of 3 ns; that value is included in the error accounting. ‘Simulated’ times refer to  $dt(D,R)$  calculated from the D and R RadioPropa-prescribed ray paths, for given source and receiver locations. Shown in Figures 12 and 14 are  $\Delta dt(D,R)$  values as a function of SPICE pulsing depth. Uncertainties in the SDP and receiver antenna coordinates on the (D,R) time differences are assessed by varying these positions in simulations, and incorporated into the  $\Delta dt(D,R)$  error bars.

As illustrated in Figure 12, the exponential model shows a trend for which measured  $dt(D,R)$  increases relative to simulated  $dt(D,R)$  at shallower depths. Even

allowing for large variations in the b and c parameters, the single exponential model still shows evident discrepancies with the SPICE  $dt(D,R)$  data. The discrepancy can be markedly reduced by using a 3 stage model, for which the  $c3$  parameter is increased in the bubbly ice region relative to the single c parameter of the single exponential. The SPICE  $dt(D,R)$  data therefore indicates that the densification rate in the bubbly ice region must be higher than what is predicted by the single exponential function.

## VII. SHADOWED ZONE

As a source moves further away laterally from a receiver or upwards to a shallower depth,  $dt(D,R)$  decreases. Eventually, as  $dt(D,R)$  approaches 0, the D and R signals seen in Figure 5 begin to overlap. Initially, this results in focusing that increases signal amplitude. However, beyond a certain point, corresponding to the shadow zone boundary, the bending of possible paths no longer allows signal to reach the receiver from the transmitter. An example of this might be a receiver that lies above the blue dashed line shown in Figure 6 relative to the deep pulser. Since refraction is determined by the  $n(z)$  model, the shadowed zone, as well as the detected neutrino rate, both depend on  $n(z)$ .

Figure 15 illustrates how changes in the refractive index model affect the lateral extent of the shadow zone. Depending on source depth, the 3 stage model changes the range to the shadow zone boundary for both a 170m and 100m depth receiver antenna, typical of antennas in the RNO-G and ARA experiments, respectively. Relative to the exponential model, the 3 stage model (Eqn. (6)) results in a reduction in the range of the shadow zone boundary for a 100m antenna and an increase of the range for a 170m antenna for South Polar ice over a range of source depths from 400m to 1000m. For source depths shallower than 200m, Eqn (6) increases the range of the shadow zone boundary. Much of the differences in the shadow zone between the two models results from the differing behaviors of the models in the firm and bubbly ice region. If the  $c3$  parameter of Eqn. (6) is instead forced to match Eqn. (5), the two shadow zone boundaries are similar.

Station A5 is located 4165m from the SPICE borehole, approximately 1km further away than the other stations. This larger lateral distance also results in an increased extent of the shadowed zone, corresponding to  $dt(D,R)$  data only being measurable over a range of 850-1300m source transmitter depth. Figure 14 shows the measured – simulated  $dt(D,R)$  results, comparing the different refractive index parameterizations for station A5. In this case, we use the  $c3$  parameter determined from A2 data and apply that value to the independent A5 dataset. The single exponential  $n(z)$  model and two stage models deviate further from measured values compared to station A2, which is improved using the 3 stage exponential  $n(z)$



model. The single and two stage models also imply a shadow zone boundary deviating from measured data.

### VIII. IMPACT ON NEUTRINO DETECTION

Overall, we observe that the three-stage model therefore results in a more restricted accessible target volume for 100m depth receiver deployments, and correspondingly decreased neutrino sensitivity. Figures 16 and 17 compare effective volume simulations using the two ice models for neutrino detector stations with 170m and 100m deep antenna deployments. The 3 stage model yields a larger effective volume than the single exponential at typical ARA station detector depths. However, the comparison reverses for more shallow antenna depths typical of other detectors.

### IX. CONCLUSION

Measured  $dt(D,R)$  time differences from deep radio-frequency transmitters support a glaciologically-motivated 3 stage exponential  $n(z)$  model over a single exponential model, which tends to overestimate  $n(z)$  in the firn region. Future analysis of the amplitude and frequency content of D and R signals can help refine the  $n(z)$  model, as phenomena such as flux focusing are also sensitive to ray curvature. More rigorous comparison of simulated shadowed zone boundaries with those extrapolated from signal amplitudes as a function of depth also provides an independent check on the refractive index profile. Additional density data in the depth range corresponding to the coefficient  $c_3$  could help to constrain the model further. An improved  $n(z)$  model should also help to provide a more accurate effective volume estimation and aid in current calibration efforts for UHEN experiments in both Greenland and the South Pole, as well as future planned experiments, such as the radio component of the IceCube-Gen2 Radio experiment.

### X. ACKNOWLEDGMENTS

Kenny Couberly was the main author of this manuscript and led the analysis discussed. The ARA Collaboration designed, constructed, and now operates the ARA detectors. We would like to thank IceCube and specifically the winterovers for the support in operating the detector; we also express our appreciation for the authors of the NuRadioMC code that was used for our simulations. Data processing and calibration, Monte Carlo simulations of the detector and of theoretical models and data analyses were performed by a large number of collaboration members, who also discussed and approved the scientific results presented here. We thank the Raytheon Polar Services Corporation, Lockheed Martin,

and the Antarctic Support Contractor for field support and enabling our work on the harshest continent. We are thankful to the National Science Foundation (NSF) Office of Polar Programs and Physics Division for funding support. We further thank the Taiwan National Science Councils Vanguard Program NSC 92-2628-M-002-09 and the Belgian F.R.S. FNRS Grant 4.4508.01. A. Connolly thanks the NSF for Award 1806923 and also acknowledges the Ohio Supercomputer Center. S. A. Wissel thanks the NSF for support through CAREER Award 2033500. M. S. Muzio thanks the NSF for support through MPS-Ascend Postdoctoral Award 2138121. A. Vieregge thanks the Sloan Foundation and the Research Corporation for Science Advancement, the Research Computing Center and the Kavli Institute for Cosmological Physics at the University of Chicago for the resources they provided. R. Nichol thanks the Leverhulme Trust for their support. K.D. de Vries is supported by European Research Council under the European Unions Horizon research and innovation program (grant agreement 763 No 805486). D. Besson, I. Kravchenko, and D. Seckel thank the NSF for support through the IceCube EPSCoR Initiative (Award ID 2019597)

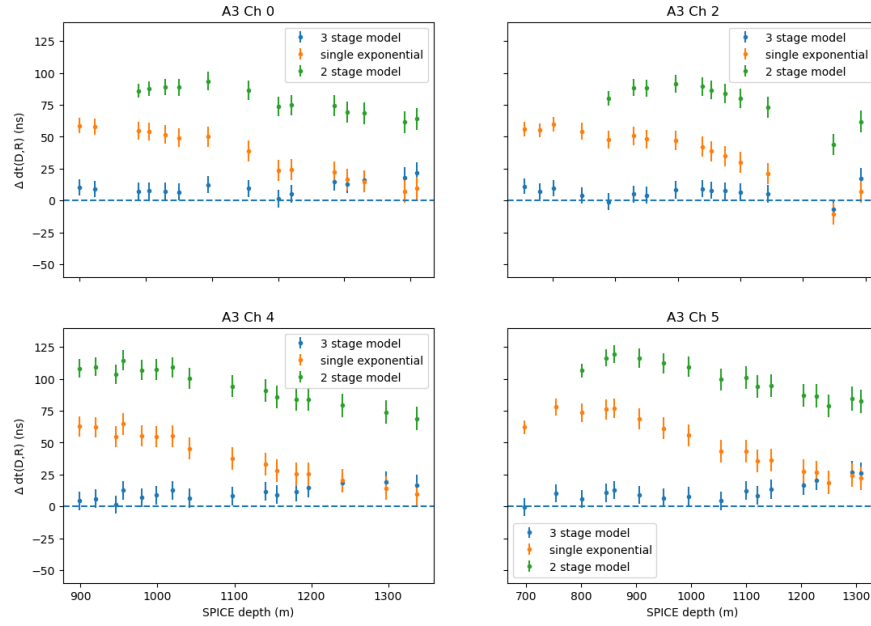


FIG. 12.  $\Delta dt(D,R)$  for signals traveling from SDP to station A3 for Vpol channels. Shown are comparisons of simulated vs measured  $dt(D,R)$  for Eqn. (5), Eqn. (6), and Eqn. (7).

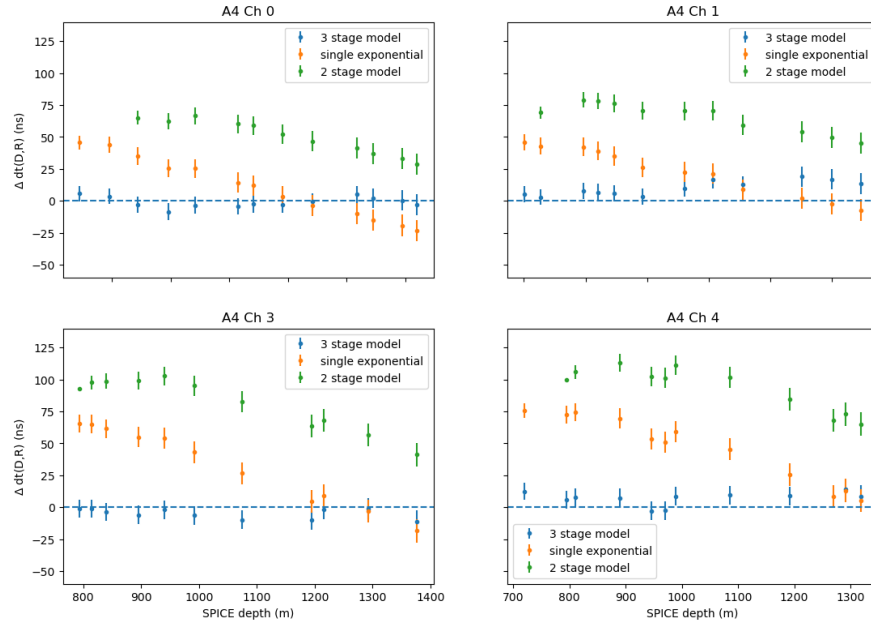


FIG. 13.  $\Delta dt(D,R)$  for signals traveling from SDP to station A3.

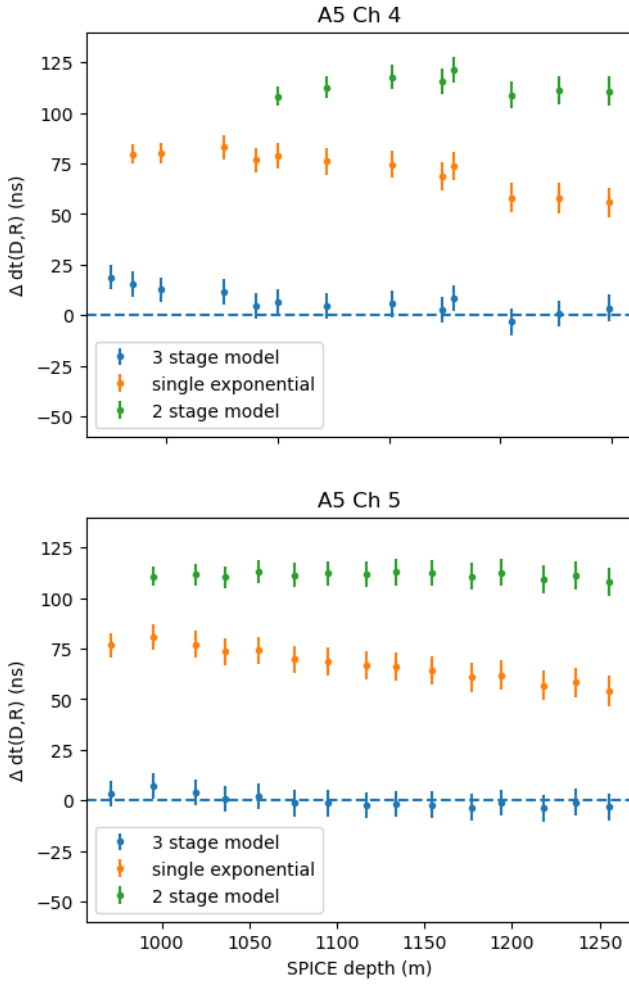


FIG. 14.  $\Delta dt(D,R)$ , extracted using Eqn. (5), Eqn. (6), and Eqn. (7) for channels 4 and 5 from station A5. The refractive index parameterization from (6) improves the agreement, relative to the single exponential model and 2 stage model fits to density data as a function of SPICE depth. A lack of simulated  $dt(D,R)$  solutions from the shadow zone of the models results in some ‘missing’ values at shallow SPICE depths for the single and 2 stage models.

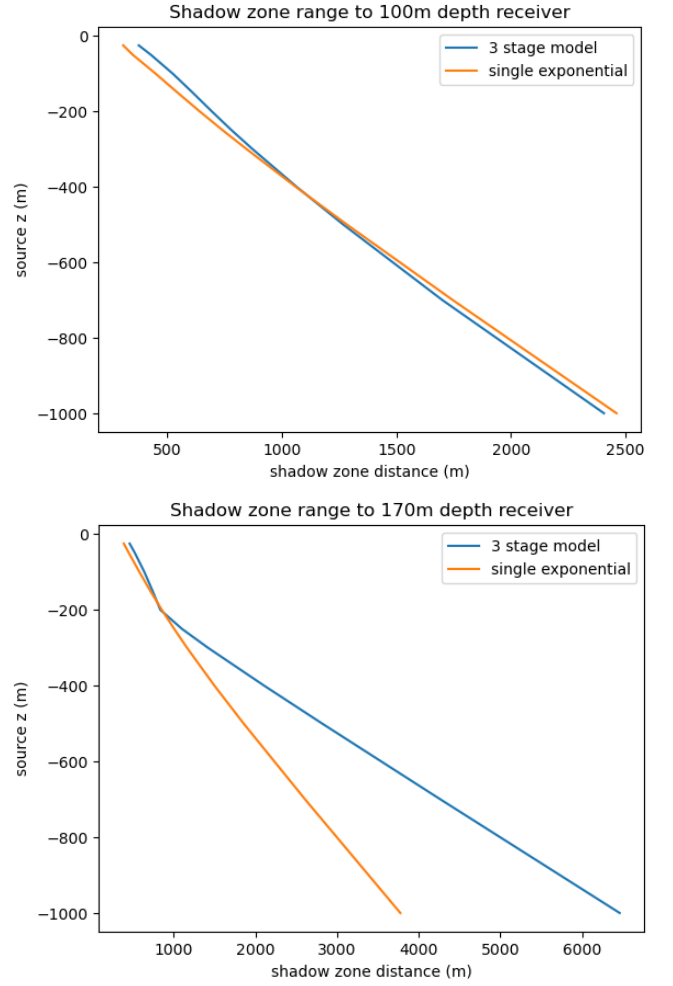


FIG. 15. Example simulated shadow zone boundary ( $r,z$ ) coordinates for 100m and 170m depth receiver antennas, for two  $n(z)$  profiles (Eqns. (5) and (6)). Over the range of the SPICE pulsing runs, antenna depths exceeding 100m, Eqn. (6) implies a smaller shadowed volume, while Eqn. (5) implies a smaller shadowed value for 170m depth typical of ARA station antennas. Eqn. (6) yields a greater shadow zone range for sources shallower than 200m depth.

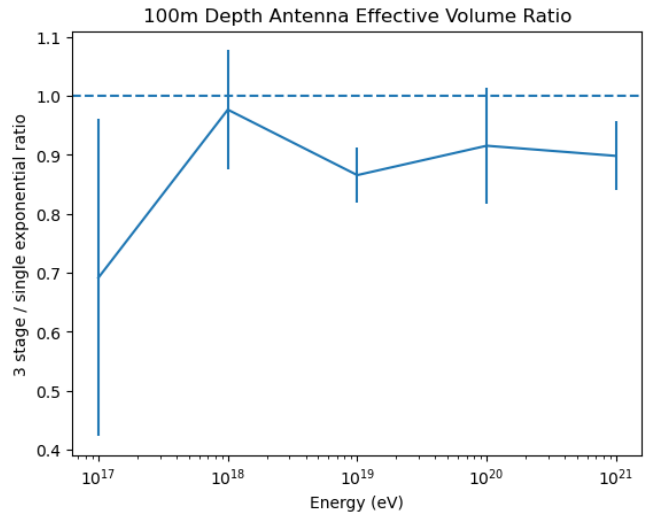
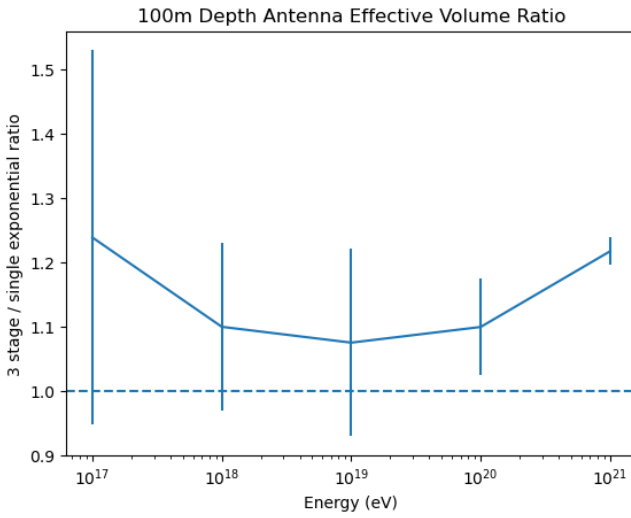
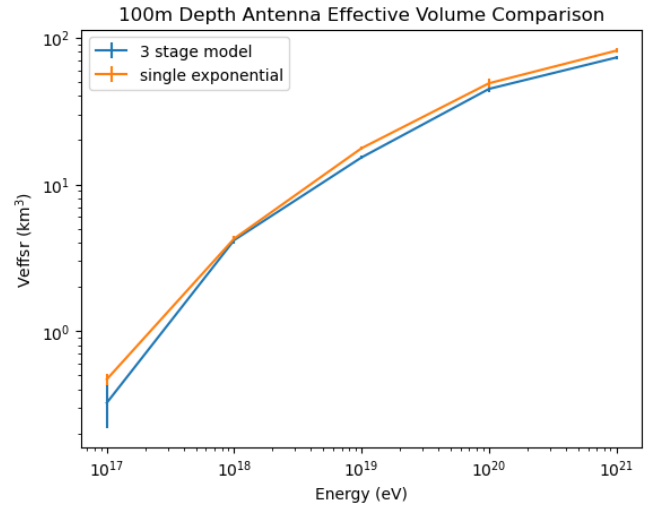
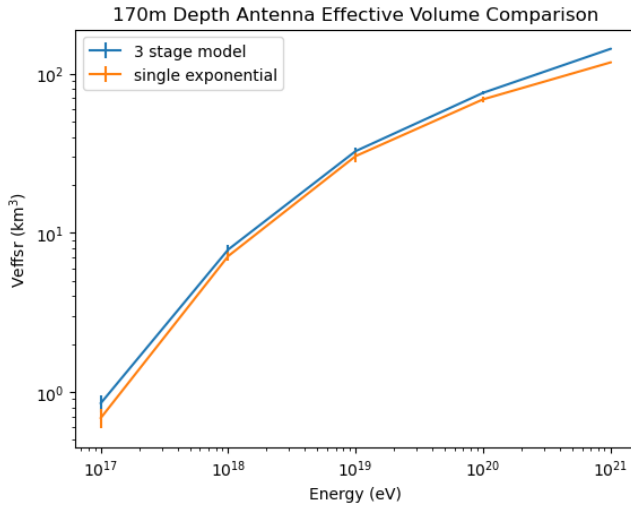


FIG. 16. Simulated effective volume (top) and ratio (bottom) plots for refractive index profiles specified by equations (5) and (6), for neutrino energies of  $10^{17}$ ,  $10^{18}$ ,  $10^{19}$ ,  $10^{20}$ ,  $10^{21}$  eV for 170m depth detector typical of ARA station. Error bars shown are statistical only.

FIG. 17. Simulated effective volume (top) and ratio (bottom) plots for 100m detector depth.

- 
- [1] Juan A Aguilar, Patrick Allison, James J Beatty, Hans Bernhoff, David Zeke Besson, Nils Bingefors, Olga Botner, Sjoerd Bouma, Stijn Buitink, Katie Carter, et al. The radio neutrino observatory greenland (rno-g). In *37th International Cosmic Ray Conference (ICRC2021)*, volume 395, 2022.
- [2] Patrick Allison, R Bard, JJ Beatty, David Zeke Besson, C Bora, C-C Chen, C-H Chen, P Chen, A Christenson, A Connolly, et al. Performance of two askaryan radio array stations and first results in the search for ultrahigh energy neutrinos. *Physical Review D*, 93(8):082003, 2016.
- [3] Mark G Aartsen, R Abbasi, M Ackermann, J Adams, JA Aguilar, M Ahlers, M Ahrens, C Alispach, P Allison, NM Amin, et al. Icecube-gen2: the window to the extreme universe. *Journal of Physics G: Nuclear and Particle Physics*, 48(6):060501, 2021.
- [4] Michael M Herron and Chester C Langway. Firn densification: an empirical model. *Journal of Glaciology*, 25(93):373–385, 1980.
- [5] C Max Stevens, Vincent Verjans, Jessica Lundin, Emma C Kahle, Annika N Horlings, Brita I Horlings, and Edwin D Waddington. The community firn model (cfm) v1. 0. *Geoscientific Model Development*, 13(9):4355–4377, 2020.
- [6] Andrey N Salamatina, Vladimir Ya Lipenkov, and Paul Duval. Bubbly-ice densification in ice sheets: I. theory. *Journal of Glaciology*, 43(145):387–396, 1997.
- [7] Valter Schytt. *Snow Studies at Maudheim: Snow Studies inland: the Inner Structure of the Ice Shelf at Maudheim as Shown by Core Drilling*. 1958.
- [8] Henri Bader. Sorge’s law of densification of snow on high polar glaciers. *Journal of Glaciology*, 2(15):319–323, 1954.
- [9] Vladimir Ya Lipenkov, Andrey N Salamatina, and Paul Duval. Bubbly-ice densification in ice sheets: II. applications. *Journal of Glaciology*, 43(145):397–407, 1997.
- [10] C. Welling and The RNO-G Collaboration. Brief communication: Precision measurement of the index of refraction of deep glacial ice at radio frequencies at summit station, greenland. *The Cryosphere*, 18(7):3433–3437, 2024.
- [11] Henri P Gavin. The levenberg-marquardt algorithm for nonlinear least squares curve-fitting problems. *Department of Civil and Environmental Engineering Duke University August*, 3, 2019.
- [12] RB Alley, CA Shuman, DA Meese, AJ Gow, KC Taylor, KM Cuffey, JJ Fitzpatrick, PM Grootes, GA Zielinski, M Ram, et al. Visual-stratigraphic dating of the gisp2 ice core: Basis, reproducibility, and application. *Journal of Geophysical Research: Oceans*, 102(C12):26367–26381, 1997.
- [13] Richard B Alley and Bruce R Koci. Ice-core analysis at site a, greenland: preliminary results. *Annals of Glaciology*, 10:1–4, 1988.
- [14] Robert L Hawley and Elizabeth M Morris. Borehole optical stratigraphy and neutron-scattering density measurements at summit, greenland. *Journal of Glaciology*, 52(179):491–496, 2006.
- [15] Robert L Hawley, Elizabeth M Morris, and Joseph R McCONNELL. Rapid techniques for determining annual accumulation applied at summit, greenland. *Journal of Glaciology*, 54(188):839–845, 2008.
- [16] Austin Kovacs, Anthony J Gow, and Rexford M Morey. The in-situ dielectric constant of polar firn revisited. *Cold Regions Science and Technology*, 23(3):245–256, 1995.
- [17] P Allison, S Archambault, JJ Beatty, DZ Besson, CC Chen, CH Chen, P Chen, A Christenson, BA Clark, W Clay, et al. Long-baseline horizontal radio-frequency transmission through polar ice. *Journal of Cosmology and Astroparticle Physics*, 2020(12):009, 2020.
- [18] C. Welling and The RNO-G Collaboration. Precision measurement of the index of refraction of deep glacial ice at radio frequencies at summit station, greenland. *The Cryosphere*, 2024.
- [19] Kimberly Ann Casey, TJ Fudge, TA Neumann, EJ Steig, MGP Cavitt, and DD Blankenship. The 1500 m south pole ice core: recovering a 40 ka environmental record. *Annals of Glaciology*, 55(68):137–146, 2014.
- [20] C. Deaconu, A. G. Vieregg, S. A. Wissel, J. Bowen, S. Chipman, A. Gupta, C. Miki, R. J. Nichol, and D. Saltzberg. Measurements and modeling of near-surface radio propagation in glacial ice and implications for neutrino experiments. *Phys. Rev. D*, 98:043010, Aug 2018. doi:10.1103/PhysRevD.98.043010. URL <https://link.aps.org/doi/10.1103/PhysRevD.98.043010>.
- [21] Uzair Abdul Latif. *Towards Measurement of UHECR with the ARA Experiment*. PhD thesis, University of Kansas, 2020.
- [22] Tobias Winchen. Radioprop — a modular raytracer for in-matter radio propagation. *EPJ Web of Conferences*, 216:03002, 2019. ISSN 2100-014X. doi:10.1051/epjconf/201921603002. URL <http://dx.doi.org/10.1051/epjconf/201921603002>.
- [23] Christian Glaser, Daniel García-Fernández, Anna Nelles, Jaime Alvarez-Muñiz, Steven W Barwick, Dave Z Besson, Brian A Clark, Amy Connolly, Cosmin Deaconu, KD de Vries, et al. Nuradiomc: Simulating the radio emission of neutrinos from interaction to detector. *The European Physical Journal C*, 80:1–35, 2020.
- [24] Matthew A Lazzara, Linda M Keller, Timothy Markle, and John Gallagher. Fifty-year amundsen-scott south pole station surface climatology. *Atmospheric Research*, 118:240–259, 2012.